High performance supercapacitors based on three-dimensional ultralight flexible manganese oxide nanosheets/carbon foam composites
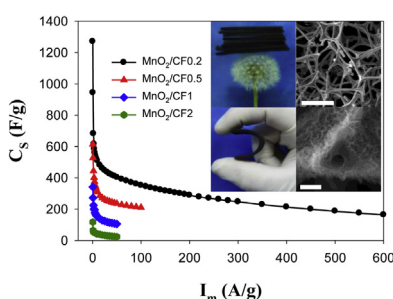
CrossMark

Shuijian He [a,b], Wei Chen [a,*]

[a] State Key Laboratory of Electroanalytical Chemistry, Changchun Institute of Applied Chemistry, Chinese Academy of Sciences, Changchun 130022, Jilin, China
[b] University of Chinese Academy of Sciences, Beijing 100039, China

HIGHLIGHTS

- Ultralight and flexible MnO_2/carbon foam (MnO_2/CF) composites are synthesized.
- Flexible carbon foam with low density is obtained by carbonizing melamine resin foam.
- MnO_2 nanosheets with a few nanometers thickness are grown on high-porous carbon foam.
- The porous MnO_2/CF can be fabricated into supercapacitor electrode without any binder.
- Supercapacitor from MnO_2/CF shows high specific capacitance and high energy density.

GRAPHICAL ABSTRACT

ARTICLE INFO

ABSTRACT

The syntheses and capacitance performances of ultralight and flexible MnO_2/carbon foam (MnO_2/CF) hybrids are systematically studied. Flexible carbon foam with a low mass density of 6.2 mg cm^{-3} and high porosity of 99.66% is simply obtained by carbonization of commercially available and low-cost melamine resin foam. With the high porous carbon foam as framework, ultrathin MnO_2 nanosheets are grown through *in situ* redox reaction between $KMnO_4$ and carbon foam. The three-dimensional (3D) MnO_2/CF networks exhibit highly ordered hierarchical pore structure. Attributed to the good flexibility and ultralight weight, the MnO_2/CF nanomaterials can be directly fabricated into supercapacitor electrodes without any binder and conductive agents. Moreover, the pseudocapacitance of the MnO_2 nanosheets is enhanced by the fast ion diffusion in the three-dimensional porous architecture and by the conductive carbon foam skeleton as well as good contact of carbon/oxide interfaces. Supercapacitor based on the MnO_2/CF composite with 3.4% weight percent of MnO_2 shows a high specific capacitance of 1270.5 F g^{-1} (92.7% of the theoretical specific capacitance of MnO_2) and high energy density of 86.2 Wh kg^{-1}. The excellent capacitance performance of the present 3D ultralight and flexible nanomaterials make them promising candidates as electrode materials for supercapacitors.

© 2014 Elsevier B.V. All rights reserved.

---

* Corresponding author. Tel.: +86 431 85262061.
  E-mail address: weichen@ciac.ac.cn (W. Chen).

1. Introduction

In recent years, a significant amount of effort has been devoted to exploring flexible and ultralight energy storage materials to meet the fast growing fashion of portable electronic devices, such as roll-up displays, electronic paper, wearable devices, mobile phones, and computers. Supercapacitors, also called electrochemical capacitors, characteristic of high power and reasonably high energy densities, currently fill the gap between batteries and conventional solid state and electrolytic capacitors [1–4]. Supercapacitors have become a versatile solution to various emerging energy applications, especially when high power delivery or uptake is needed. Supercapacitors can store energy either by ion adsorption (electrochemical double layer capacitors, EDLCs) or by fast surface redox reactions (pseudocapacitors) in nature [5]. EDLCs mainly use various carbon nanomaterials as electrode materials. EDLCs often display relatively low specific capacitance (Cs) and energy densities but high power densities [6]. In contrast, pseudocapacitors which store energy via redox reactions of electroactive materials, like conducting polymers and transition metal oxides/hydroxides, possess opposite properties [7].

In order to explore electrode materials with both high energy densities and power densities, much work has been done on integrating active materials on 3D self-supported substrates [8–16], especially on light and flexible carbon skeletons including reduced graphene oxide gel/foam, carbon foam/paper/cloth, carbon nanotube arrays/film, etc [17–23]. These composites have many advantages when used as supercapacitor electrode materials. First, with these materials, no binder is needed for constructing supercapacitor electrodes, which simplify the electrode preparing process. The usually used binders which often raise the electrode resistance and lead to low power density are indispensable during electrode preparing. Therefore, supercapacitors based on binder-free electrode materials usually show relatively higher power densities and better rate capacitance performance [24,25]. Second, 3D carbon substrates can not only avoid the aggregation of capacitance-active materials but also facilitate the electron transfer during charge/discharge process which ensures full use of the active materials [26,27]. Moreover, Due to the large porosity (>90%) and high conductivity of the ultralight carbon materials, the 3D porous structures are very beneficial for electrolyte diffusion and electron transfer. Therefore, supercapacitors based on these flexible and lightweight carbon materials always show excellent rate capacitance performance and stability. Previous studies showed that by depositing active materials like MnO_2 on the ultralight carbon materials, the specific capacitance and energy density of the hybrids can be greatly improved, which makes them promising candidates for flexible, ultralight energy storage materials [8,23].

However, the preparation of ultralight carbon materials is usually time-consuming and complicated. There are mainly two ways to fabricate the ultralight carbon support materials. One is that graphene/carbon nanotube hydrogels are first prepared through hydrothermal self-assembly of graphene or carbon nanotube. The hydrogels are then dried via freeze drying/lyophilization to get aerogels [17,18]. In another way, graphene layers or carbon nanotube array/sponge can be directly grown on various substrates through chemical vapor deposition, followed by removing substrates [8,28]. Both methods not only take time and need critical preparation conditions, but also produce only small-scale output. Therefore, it is still an urgent and important issue to explore facile methods to prepare flexible and ultralight energy storage materials with large-scale production and low cost.

In this paper, ultralight and flexible carbon foam (CF) with low density of 6.2 mg cm^{-3} was simply synthesized through carbonizing commercial melamine resin foam (MRF) with low cost and

large-scale production. This novel carbon foam is quite different from other resin-derived 3D porous carbon foams/monoliths/aerogels in the preparation, porous structure, density and flexibility. Traditionally, carbon foams/monoliths/aerogels were prepared by carbonizing blends of phenolic resins and templates like silica spheres, Zeolite Y, polystyrene spheres and block copolymers [29–31]. The removable, expensive polymer latex, silica, or other colloidal particles are energy-consuming and uneconomic, and the synthesis procedure is complicated and time-consuming [32]. What is more, the output and the processability of these carbon materials are largely limited. In this study, a type of large-scale producible and flexible carbon foam can be easily obtained from direct carbonization of low-cost melamine foam. The density of the carbon foam is comparable to other ultralight aerogel/foam/sponge-like materials, like graphene foam/aerogels and CNT sponges [28,33–38]. Meanwhile, the prepared carbon foam can serve as an excellent 3D porous framework to fabricate ultralight supercapacitor electrode due to its low density and high flexibility. To the best of our knowledge, this is the first report of 3D supercapacitor fabricated from melamine resin-derived composite. Here, MnO_2 nanosheets/CF composites were prepared by *in situ* reaction between $KMnO_4$ and carbon and functioned as ultralight and flexible supercapacitor electrode materials for the first time. The electrochemical studies indicated that the as-prepared coaxial composites showed excellent capacitance performance. The highest specific capacitance of MnO_2 could reach 1270.5 F g^{-1} which is 92.7% of its theoretical specific capacitance (1370 F g^{-1}) [39]. Moreover, the supercapacitor fabricated with the present 3D network materials exhibited high energy density of 86.2 Wh kg^{-1}, high power density of 160.0 kW kg^{-1} and also high stability. Overall, this research provides a simple and efficient method for preparing MnO_2/CF composites from the low-cost and large-scale available melamine resin foam. With the advantages of easy fabrication, low cost, lightweight, high flexibility and excellent capacitance performance, the fabricated 3D porous MnO_2/CF hybrids represent a class of promising electrode materials for supercapacitors.

2. Experimental

All the reagents used in the experiments were analytical grade and were used without further purification.

2.1. Preparation of carbon foam

Carbon foam was prepared by carbonizing melamine resin foam (MRF, supplied by Puyang Green Universh Chemical Co., Ltd.) under Ar flow of 100 mL min^{-1}. MRF was cut into pieces with size of 0.5 cm × 3.5 cm × 25 cm before carbonization. The carbonization process is as follows: the temperature was first raised from room temperature to 300 $^{\circ}$C at a rate of 5 $^{\circ}$C min^{-1} and kept for 5 min; in the next step, the temperature was further raised to 400 $^{\circ}$C at a rate of 1 $^{\circ}$C min^{-1} and kept for 5 min; finally, the temperature was raised to 1000 $^{\circ}$C at a rate of 3 $^{\circ}$C min^{-1} and kept for 1 h.

2.2. Fabrication of MnO_2/carbon foam composites (MnO_2/CF)

After carbonization, carbon foam retained one eighth of the size of the pre-carbonization MRF. We found that in order to improve the hydrophilicity of the prepared carbon foam, it should be soaked in ethanol first and then washed with abundant deionized water to remove ethanol, otherwise, it can hardly infiltrated by $KMnO_4$ aqueous solution. 55 mg of the pre-treated carbon foam was immersed in a 200 mL $KMnO_4$ aqueous solution in a glass bottle. The bottle was then put into a water bath at 60 $^{\circ}$C until the purple

color of $KMnO_4$ disappeared. Finally, the products were collected, rinsed with deionized water and dried at 60 °C. A series of MnO_2/CF 3D porous materials were prepared by controlling the concentration of $KMnO_4$ aqueous solution from 0.2, 0.5, 1 to 2 mM. The composites are denoted as MnO_2/CF0.2, MnO_2/CF0.5, MnO_2/CF1 and MnO_2/CF2, respectively.

2.3. Material characterization

The contact angle of carbon foam was measured by a DSA100 drop shape analysis instrument (DSA, KRÜSS GMBH). The weight percentages of MnO_2 in the series of composites were calculated from thermogravimetric analysis (TGA, Pyris Diamond TG/DTA), which was carried out under air flow of 60 mL min^{-1} with a heating rate of 5 °C min^{-1}. The morphologies of the samples were examined by scanning electron microscopy (SEM; XL30) and transmission electron microscopy (TEM; Hitachi H-600). High-resolution TEM (HRTEM) images, X-ray energy dispersive spectroscopy (EDS) and the selected area electron diffraction (SAED) were carried out on a JEM-2010(HR) microscope. The crystal structures of the as-prepared products were characterized by an X-ray powder diffractometer (XRD; D/Max 2500 V/PC, Cu-Kα radiation) with a scan speed of 2° min^{-1}. Raman spectra were collected through a Renishaw 2000 model confocal microscopy Raman spectrometer with a CCD detector and a holographic notch filter (Renishaw Ltd., Gloucestershire, U.K.) at ambient conditions, using the radiation of 514.5 nm from an air-cooled argon ion laser to excite the SERS. X-ray photoelectron spectroscopy (XPS) measurements were performed on a VG Thermo ESCALAB 250 spectrometer (VG Scientific) operated at 120 W with an energy analyzer working in the pass energy mode at 100.0 eV. An Al Ka line was used as the excitation source. The binding energy was calibrated against the carbon 1s line. Nitrogen sorption isotherms were measured at 77 K on an automatic N_2 adsorption/desorption instrument (Quantachrome Autosorb Automated Gas Sorption System) and the samples were outgassed in vacuum at 200 °C for 8 h before test. The specific surface areas of the materials were calculated by the Brunauer–Emmett–Teller (BET) method using the adsorption branch in the relative pressure range from 0.05 to 0.35. The pore size distributions were derived from the adsorption branch using the Barrett–Joyner–Halenda (BJH) model. The total pore volume was determined from the amount of N_2 uptake at $P/P_0 = 0.99$.

2.4. Electrochemical measurements

The working electrodes were prepared by pressing pieces of the as-synthesized materials with the same weight (1.0 mg) sandwiched between two pieces of Ni foams under 10 MPa. 1.0 M Na_2SO_4 aqueous solution was used as electrolyte. Electrochemical measurements were all conducted on a CHI 660D electrochemical workstation (Shanghai, Chenhua). Cyclic voltammogram (CV) and electrochemical impedance spectroscopy (EIS) measurements were carried out via a three-electrode cell with a graphite plate functioned as counter electrode and an Ag/AgCl electrode (saturated with KCl (aq)) acted as reference electrode. EIS was tested in the frequency range of 100 kHz to 10 mHz. Galvanostatic charge–discharge measurements (GCD) were carried out between 0 and 0.7 V in a symmetrical two-electrode system.

Specific capacitance C_s (F g^{-1}), energy density W (Wh kg^{-1}) and power density P (kW kg^{-1}) were calculated from GCD curves according to the equations as follows [40]:

$$C_s = 2I\Delta t/(m\Delta V) \tag{1}$$

$$W = 0.5 \times C_m \times \Delta V^2 \tag{2}$$

$$P = W/\Delta t \tag{3}$$

where I is the charge–discharge current, m is the mass of MnO_2 in a single electrode, Δt is the discharge time, and ΔV is the potential drop during the discharge process (IR drop not included).

3. Results and discussion

3.1. Synthesis and characterization of materials

Melamine resin foam (MRF) is a type of commercially available and low-cost ultralight material, and has been widely applied in shock/sound absorption, heat insulation/preservation, aviation, automobile industry and other fields due to its good physical properties. In the present study, we found that flexible, ultralight and highly porous carbon foam (CF) can be easily obtained through carbonization of MRF. Fig. 1A shows the photographs of MRF, CF and MnO_2/CF composites containing different contents of MnO_2. It can be seen that the original white MRF changed to gray carbon foam after carbonization with a low carbon yield of 8.9%. With the content of MnO_2 in the MnO_2/CF composites increasing, the color of the materials changed gradually into dark brown. Moreover, both carbon foam and MnO_2/CF composites all retained the original foam-like shape of MRF. It should be noted that the obtained 3D MnO_2/CF networks are ultralight. From the data listed in Table S1, CF and MnO_2/CF composites have very low mass density with the range from 6.2 to 10.5 mg cm^{-3}. As shown in Fig. 1B, due to the ultra-low mass density of the MnO_2/CF composites, a fragile dandelion sphere could even support a pile of MCF0.5 with volume of 14.6 cm^3 without deformation. More importantly, such porous materials show good flexibility and super mechanical strength, as shown in Fig. 1C. The ultralow mass density of the obtained MnO_2/CF materials could be attributed to the high porosity of MRF and low carbon yield after carbonization. Fig.1D–F shows the morphologies and structures of the MRF precursor, carbon foam and the as-synthesized 3D MnO_2/CF network. Clearly, after MnO_2 nanosheets grown on the carbon foam framework, the highly porous structure is well retained and all of the foam-like materials are composed of triangle fibers which interconnected and formed plenty of micron-sized pores, resulting in network architectures. Meanwhile, there are also a lot of holes in the carbon fibers which can be seen in the cross section view of the materials (Fig. S1). These holes can further reduce the mass density and increase the porosity of CF and MnO_2/CF composites. The porosity of carbon foam is as high as 99.66% calculated by the equation proposed by Chen et al. [41,42]. On the other hand, hydrophilicity of a material is very important for its application in supercapacitors. The hydrophilicity of the prepared materials was first studied. It can be seen from Fig. S2 that the as-prepared carbon foam could float on water surface without being wetted and the contact angle of carbon foam was measured to be 133° (Fig. S2C), indicating the strong hydrophobicity of the as-synthesized carbon foam. After reacting with $KMnO_4$, the resulted MnO_2/CF porous materials, however, showed excellent hydrophilicity and could be infiltrated once they were put into water as showed in Fig. S2A. The unique porous structures and excellent hydrophilic properties make the MnO_2/CF 3D networks promising supercapacitor materials.

The morphologies and compositions of the MnO_2/CF hybrids were analyzed by SEM and thermogravimetric analysis (TGA). Fig. 2 shows the SEM images of the MnO_2/CF0.2 (A, B), MnO_2/CF0.5 (C, D), MnO_2/CF1 (E, F) and MnO_2/CF2 (G, H), respectively. It can be seen that after *in situ* reaction with $KMnO_4$, a uniform layer of MnO_2
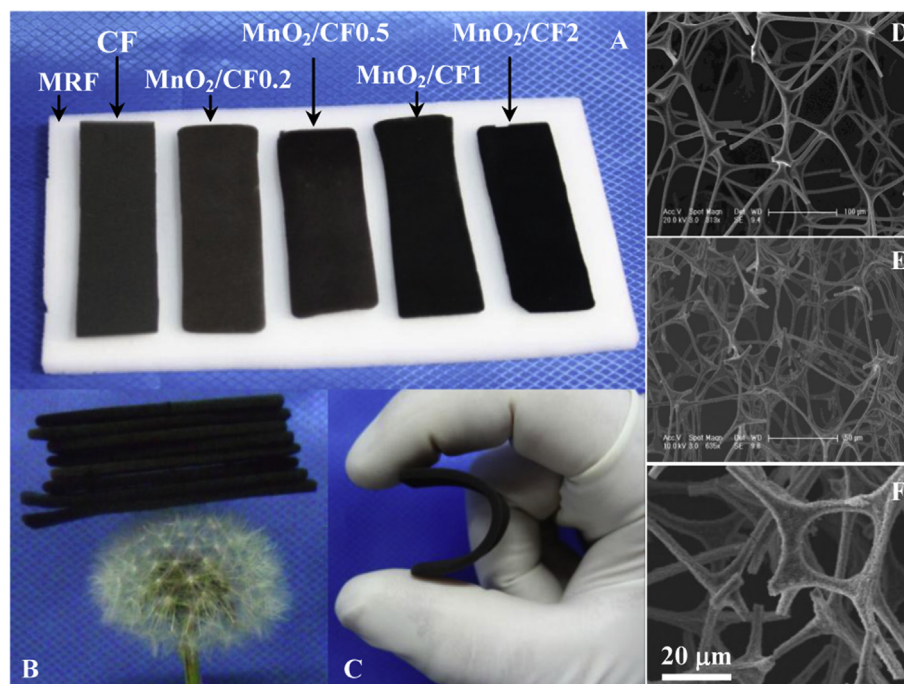
Fig. 1. (A) Photographs of melamine resin foam (MRF), carbon foam (CF) and MnO$_2$/CF composites with different MnO$_2$ content. (B) Digital photograph of a pile of MnO$_2$/CF1 on a fragile dandelion sphere, showing the ultralight performance of the synthesized 3D MnO$_2$/CF composites. (C) Digital photograph of a piece of MnO$_2$/CF1, indicating the high flexibility of the obtained MnO$_2$/CF materials. (D–F) SEM images of MRF (D), CF (E) and MnO$_2$/CF2 (F), showing the highly porous 3D networks.

nanosheets is tightly adhered to the surface of the carbon form, forming a coaxial structure. The weight percents of MnO$_2$ in the MnO$_2$/CF0.2, MnO$_2$/CF0.5, MnO$_2$/CF1 and MnO$_2$/CF2 were calculated to be 3.4%, 7.7%, 10.9% and 24.5%, respectively, according to the TGA measurements shown in Fig. S3. The TGA results indicate that the content of MnO$_2$ in the resulting hybrids increases with increasing the concentration of KMnO$_4$ during the syntheses. Moreover, from the SEM images shown in Fig. 2, both of the thickness of the MnO$_2$ layers and the size of MnO$_2$ nanosheets increase with the KMnO$_4$ concentration increasing. The produced MnO$_2$ nanosheets are only a few nanometers in thickness and have numerous wrinkles and ripples which form numerous nanoscale channels (Fig. 2 and Fig. 3A). Such hierarchical pore structure, including micron-sized pores of carbon foam and nanoscale channels among MnO$_2$ nanosheets, can effectively improve the surface/interface area of MnO$_2$ nanocrystals and facilitate electrolyte diffusion among interspaces of MnO$_2$ nanosheets. The 3D porous MnO$_2$/CF hybrid materials synthesized by the present route are beneficial for the full utilization of MnO$_2$ nanosheets and enhancing their rate capacitance performance.

The pore structure of the materials was further probed using the nitrogen sorption technique. Fig. S4 shows the nitrogen sorption isotherms and the pore size distribution of the MnO$_2$/CF materials. From the isotherm curves shown in Fig. S4A, the uptakes at low relative pressures ($P/P_0 < 0.05$) are very low, suggesting a limited microporosity. However, significantly increased uptakes can be observed at higher relative pressures ($0.05 < P/P_0 < 1$), indicating the porosity in the meso- and macro-range. As illustrated in Fig. S4B, the pore size is mainly distributed in the range of 2.0–7.5 nm. Note that there are also many pores with the size above 7.5 nm but few pores below 2 nm, which is consistent with the results of the nitrogen sorption isotherms. The data of the specific surface area (S_A), total pore volume and average pore size are listed in Table S1. The S_A of the MnO$_2$/CF products is much larger than that of the CF. However, the S_A of the MnO$_2$/CF is not proportional to the

MnO$_2$ content, which would be due to the different size and thickness of MnO$_2$ nanosheets in the samples. With the low MnO$_2$ content of 3.4%, the S_A of the MnO$_2$/CF0.2 was calculated to be 69.6 m^2 g^{-1} which was about three times of that of the carbon foam. To evaluate the specific surface area from only MnO$_2$ nanosheets, the specific surface area based on the mass of MnO$_2$ (S_M) was also calculated. As shown in Table S1, the S_M data from MnO$_2$/CF0.2, MnO$_2$/CF0.5, MnO$_2$/CF1 and MnO$_2$/CF2 were measured to be 1358.3, 1821.3, 1179.7 and 512.9 m^2 g^{-1}, respectively. It can be seen that the S_M of the MnO$_2$/CF composites first increases and then decreases with increasing the concentration of KMnO$_4$ solution, which could be attributed to the different structures of the composites. From the above SEM and TGA measurements, although the content of MnO$_2$ in the composites increases with increasing the concentration of KMnO$_4$, both the size of the formed MnO$_2$ nanosheets and the thickness of MnO$_2$ layer on carbon foam increase with KMnO$_4$ concentration, which could result in the decreased specific surface area. The large values of S_M can guarantee the full utilization and high specific capacitance of MnO$_2$ nanosheets.

The crystal structure of the MnO$_2$ nanosheets was characterized by high-resolution TEM (HRTEM) measurements. From the HRTEM image shown in Fig. 3A, the formed MnO$_2$ nanosheets exhibit porous and wrinkled structure. Upon careful HRTEM analysis on a piece of MnO$_2$ nanosheet (Fig. 3B), the well-resolved lattice fringes with interplanar spacing of 0.25 nm can be observed, which can be indexed to the (101) plane of birnessite-type MnO$_2$ [43,44]. The selected area electron diffraction (SAED) pattern shown in Fig. 3C displays a polycrystalline feature due to the random orientation of different MnO$_2$ nanocrystals. The X-ray energy dispersive spectroscopy (EDS) result in Fig. 3D demonstrates that the as-prepared composites mainly contain C, Mn, and O elements. The signal of potassium is possibly from KMnO$_4$ since there is always a possibility of potassium ions co-existing in the MnO$_2$ matrix [45,46]. The crystalline structure of the MnO$_2$ nanosheets was further identified by XRD measurements. As shown in Fig. 4A, for the carbon foam,
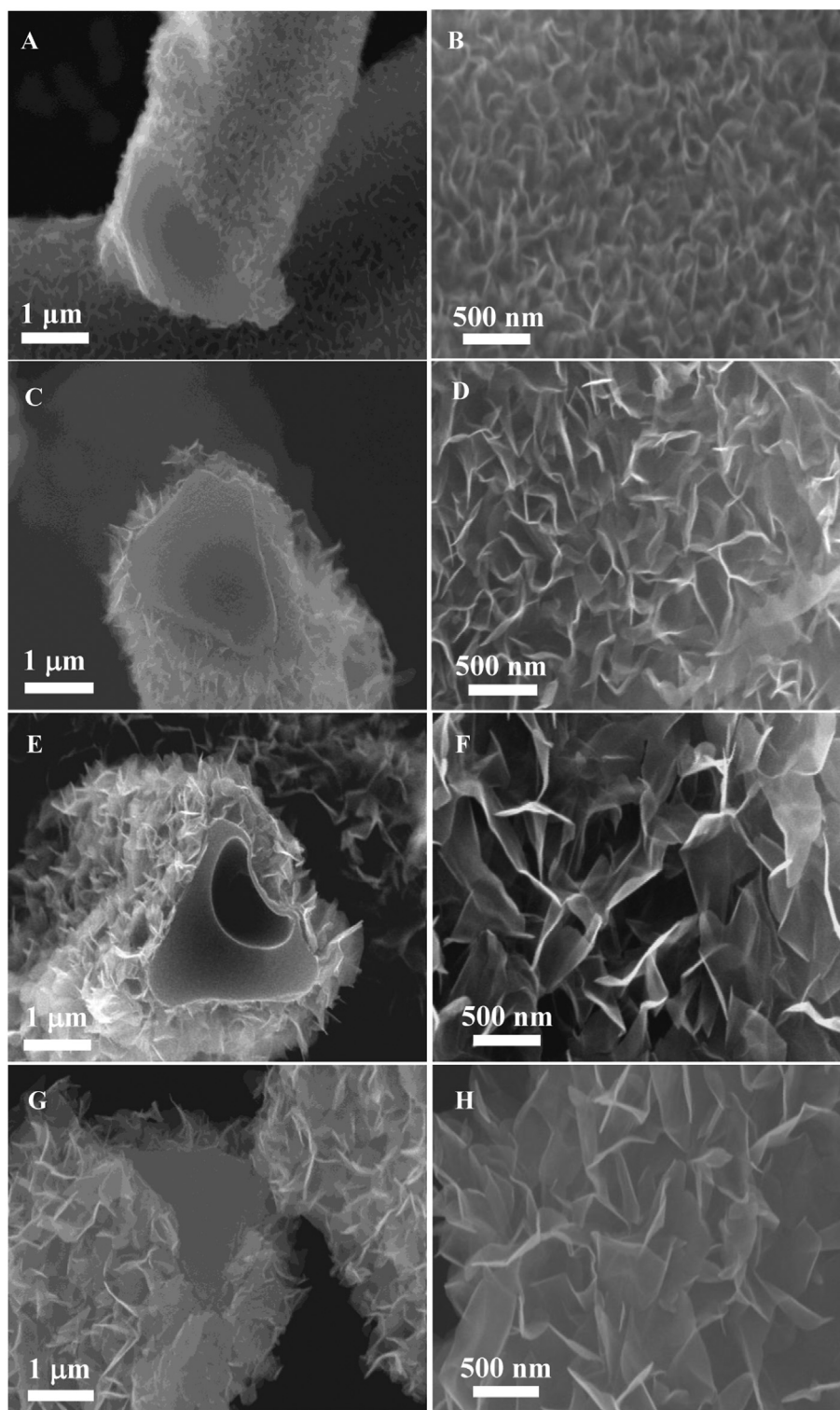
Fig. 2. Cross section (left panels) and top (right panels) SEM views of the $MnO_2/CF0.2$ (A, B), $MnO_2/CF0.5$ (C, D), $MnO_2/CF1$ (E, F) and $MnO_2/CF2$ (G, H).

there are two broad diffraction peaks with 2θ around $25°$ and $44°$, which can be ascribed to the (002) and (100) planes of amorphous carbon. For MnO_2/CF composites, except for the signals from CF, several new diffraction peaks can be observed with 2θ around $12°$, $25°$, $37°$ and $66°$, corresponding to the (001), (002), (111) and (020) diffraction of birnessite-type MnO_2 crystalline phase (JCPDS no.42-1317) [47,48]. Meanwhile, with the increasing of $KMnO_4$

concentration in the syntheses, the diffraction peaks belonging to MnO_2 become stronger and the intensities of the diffraction peaks from CF decrease, suggesting the increase of MnO_2 content from $MnO_2/CF0.2$ to $MnO_2/CF2$. The Raman spectra of carbon foam and the MnO_2/CF composites are shown in Fig. 4B. The two peaks at about 1369 and 1590 cm^{-1} are ascribed to the D- and G-band of carbon materials, respectively. G-band is assigned to the stacking of
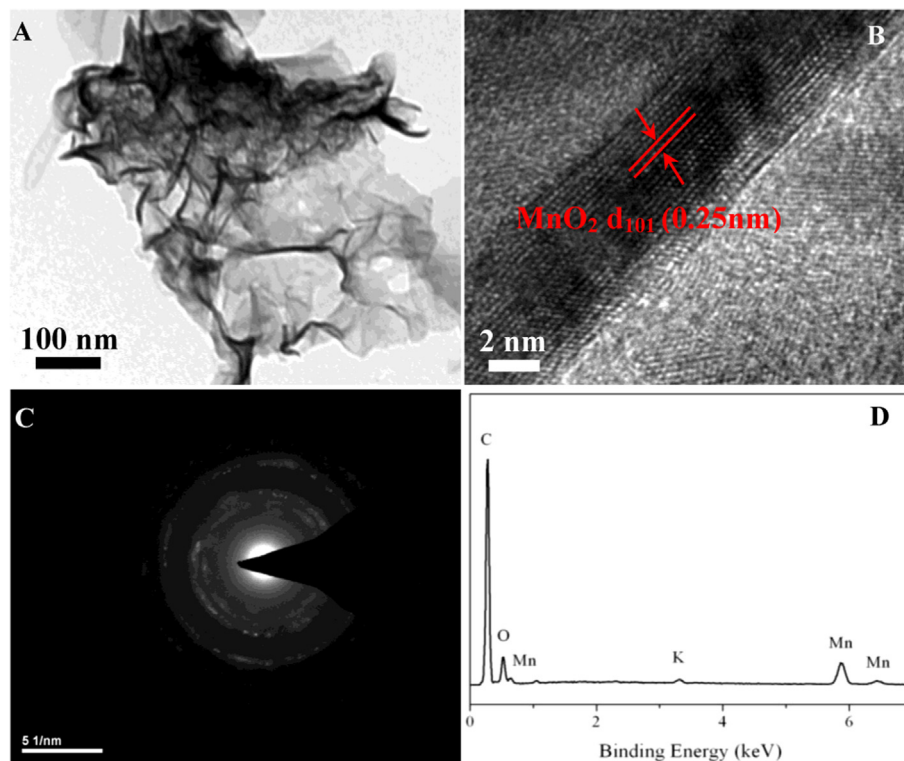
Fig. 3. (A, B) HRTEM images of MnO$_2$ nanosheets stripped from MnO$_2$/CF0.2 at different magnifications. (C) Selected area electron diffraction (SAED) pattern and (D) energy dispersive spectroscopy (EDS) spectrum of the MnO$_2$/CF0.2.

the graphite hexagon network plane, whereas D-band is attributed to the amorphous carbon or deformation vibrations of a hexagonal ring. It is accepted that the intensity ratio of the G and D bands (I_G/I_D) can give the useful information on the graphite degree or the lattice distortion of carbon-based materials. The larger the ratio is, the higher the graphitization is [49]. The I_G/I_D of carbon foam was calculated to be 1.25 from Fig. 4B, indicating the relatively high graphitization of the as-obtained carbon material at a carbonization temperature of 1000 °C. As for the MnO$_2$/CF composites, three additional bands from MnO$_2$ nanosheets can be observed at 490, 568, and 646 cm^{-1} [50]. It should be noted that with the increasing of KMnO$_4$ concentration in the syntheses, the bands belonging to MnO$_2$ become more and more distinct and the intensity ratio of the bands from MnO$_2$ and carbon foam also increases, which further suggests the increase of MnO$_2$ content in the composites. The XPS survey on sample of MnO$_2$/CF0.5 is shown in Fig. 5. Agreeing well with the EDS results, the XPS signals from elements C, Mn and O can be observed in Fig. 5A. Fig. 5B shows the Mn 2p core-level XPS spectrum. The binding energies of Mn 2p$_{3/2}$ and 2p$_{1/2}$ located at about 642.1 and 653.8 eV, respectively, with a spin-energy separation of 11.7 eV, suggesting that the predominant oxidation state of Mn is +4 [51–53].

3.2. Electrochemical capacitance performance of MnO$_2$/CF composites

To investigate the potential application of the as-obtained 3D MnO$_2$/CF composites as supercapacitor electrode materials, the composites sandwiched in Ni foams were characterized by cyclic voltammogram (CV) and galvanostatic charge–discharge (GCD) measurements at varied scan rates and current densities. As shown in Fig. 6A, the CV curves of all the MnO$_2$/CF samples are almost ideally rectangular at potential scan rate of 5 mV s^{-1}. This is due to

the surface electrosorption of electrolyte cations and the fast, reversible successive surface redox reactions of MnO$_2$ by means of intercalation/de-intercalation processes of the cations (C$^+$ = H$^+$, Li$^+$, Na$^+$ and K$^+$) according to the following reaction [39,54]

$$MnO_2 + C^+ + e^- \Leftrightarrow MnOOC \qquad (4)$$

The absence of redox peaks indicates that the supercapacitors are charged and discharged at a pseudo-constant rate over the entire voltammetric cycles [26].

By comparing the integral areas of CV curves, the carbon foam substrate shows a negligible capacitance compared to the MnO$_2$/CF composites, which can be ascribed to its strong hydrophobicity (Fig. S2) and low specific surface area. Therefore, the capacitances of the MnO$_2$/CF composites mainly originate from the pseudocapacitance of MnO$_2$ nanosheets, and the CF acts only as flexible electric conductivity scaffold. Based on these results, the weight of carbon foam was not taken into account for the specific capacitance calculations in the present study. Among the CVs of MnO$_2$/CF materials, one can see that the current density and the integration area of CV curve obtained from MnO$_2$/CF0.2 are significantly larger than those of the other MnO$_2$/CF samples, suggesting the largest capacitance of MnO$_2$/CF0.2. As aforementioned, the size of the MnO$_2$ nanosheets increases in the order of MnO$_2$/CF0.2 < MnO$_2$/CF0.5 < MnO$_2$/CF1 < MnO$_2$/CF2. Although the specific surface area of MnO$_2$ in MnO$_2$/CF0.5 (1821.3 m^2 g^{-1}) is larger than that of MnO$_2$/CF0.2 (1358.3 m^2 g^{-1}), the specific capacitance of MnO$_2$/CF0.5 is smaller than that of MnO$_2$/CF0.2 due to relatively larger size of MnO$_2$ nanosheets which lead to larger resistance and lower utilization ratio of MnO$_2$. Thus the high capacitance performance of MnO$_2$/CF0.2 could be ascribed to its small and ultrathin nanosheet structure which can not only enlarge the surface area of MnO$_2$ nanosheets, but also increase the contact area with carbon foam and thus accelerate the electron transfer. In the present study, the
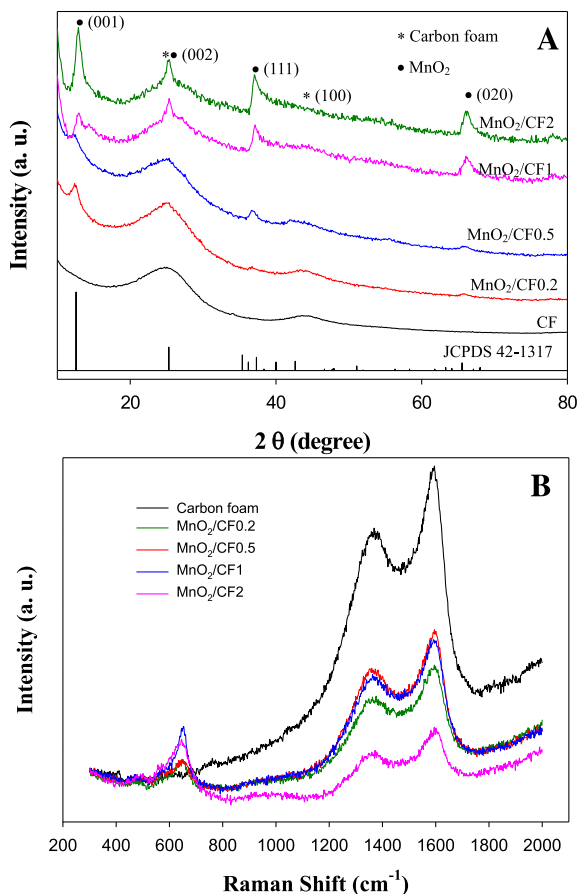
Fig. 4. XRD patterns (A) and Raman spectra (B) of the carbon foam (CF) and MnO_2/CF composites.

MnO_2 nanosheets grow epitaxially on the surface of carbon foam, which allows easy and efficient access of both electrons and ions so as to afford a fast redox reaction at high scan rates. As shown in Fig. 6B, the MnO_2/CF electrodes show excellent rate capacitance performance as they could undergo high scan rate of 1 V s^{-1}. More importantly, the scan rate for MnO_2/CF0.2 could be even increased to 5 V s^{-1} (Fig. S5). It should be noted that the resistance of the composites could increase with the MnO_2 content increasing. It can be seen from Fig. 6A that higher polarization occurs at high potentials with the increasing of MnO_2 content in the composites. It is also clear from Fig. 6B that the CV curves of the MnO_2/CF

composites gradually change from rectangular to oval shapes with the increasing of MnO_2 content, which is due to the low electric conductivity of MnO_2.

The GCD curves of the supercapacitors based on MnO_2/CF composites at current densities of 5 and 80 A g^{-1} are shown in Fig. 6C and D, respectively. The symmetric and near linear charge/discharge curves at both current densities reveal the excellent electrochemical reversibility and charge–discharge properties of the MnO_2/CF-based supercapacitors with a rapid I–V response. It is worth noting that the supercapacitors based on the composites could undergo current density as high as 80 A g^{-1}, which suggests their outstanding rapid charge-discharge performance. Moreover, as shown in Fig. S6, the MnO_2/CF0.2 electrode could even endure current density up to 600 A g^{-1} with a charge-discharge cycle shorter than 0.32 s, which well meets the short time requirement of practical supercapacitors. On the other hand, the increased IR drop at the beginning of discharge process displayed in Fig. 6D suggests that the resistance of the electrodes increases with the MnO_2 content in the MnO_2/CF composites. Such result agrees well with that from the CV measurements. The specific capacitances (C_s) of the four samples at different current densities (I_m, A g^{-1}) were calculated by Equation (1) ($C_s = 2I\Delta t/(m\Delta V)$ in Experimental Section) and displayed in Fig. 7A. By comparing the curves obtained from different samples, the MnO_2/CF0.2 exhibits the largest C_s among all the composites with 1270.5 F g^{-1} at 0.5 A g^{-1}. Even at the high current density of 600 A g^{-1}, the MnO_2/CF0.2 still retains a relatively high C_s of 162.8 F g^{-1}. The excellent rate capacitance performance could be attributed to three reasons. First, the 3D self-supported carbon foam scaffold can avoid the use of binder and thus guarantee the full utilization of MnO_2 nanosheets. Second, the hierarchical porous structure of the hybrid networks, including the micro-sized macropores of carbon foam and the nano-sized interspace among MnO_2 nanosheets, is favorable for electrolyte immersion and diffusion. Finally, the ultrathin and wrinkled structure of MnO_2 nanosheets is beneficial for preventing aggregation of MnO_2 nanosheets and improving their available surface area. As listed in Table 1, the MnO_2/CF0.2 exhibits the largest specific capacitance compared to other hybrid composites. From the charge–discharge curves, energy density (W) and power density (P) can also be obtained. As displayed in Fig. 7B, the MnO_2/CF0.2 has an energy density of 86.2 Wh kg^{-1} at power density of 174.8 W kg^{-1} and the energy density of 6.4 Wh kg^{-1} still can be retained even when the power density reaches 160.0 kW kg^{-1} at a large current density of 600 A g^{-1}, indicating the excellent rate performance and high power density of the 3D hybrid materials.

The facilitated ion-transport kinetics and electrode conductivity of the synthesized MnO_2/CF composites were further confirmed by
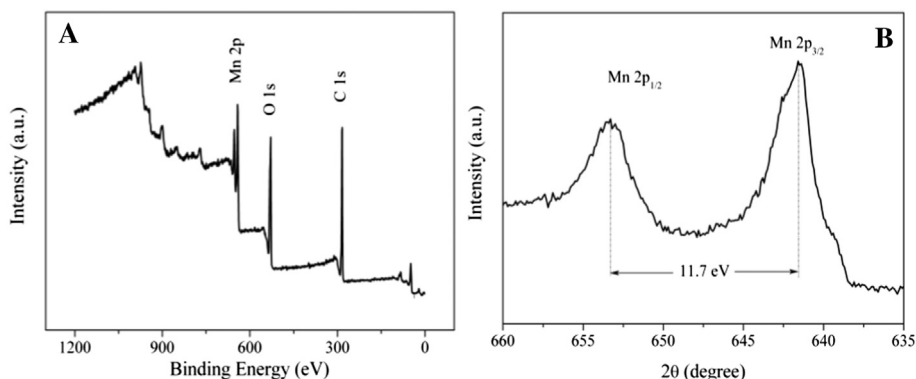
Fig. 5. XPS spectra of MnO_2/CF0.2. (A) Survey spectrum; (B) the core-level XPS signals of Mn 2p.
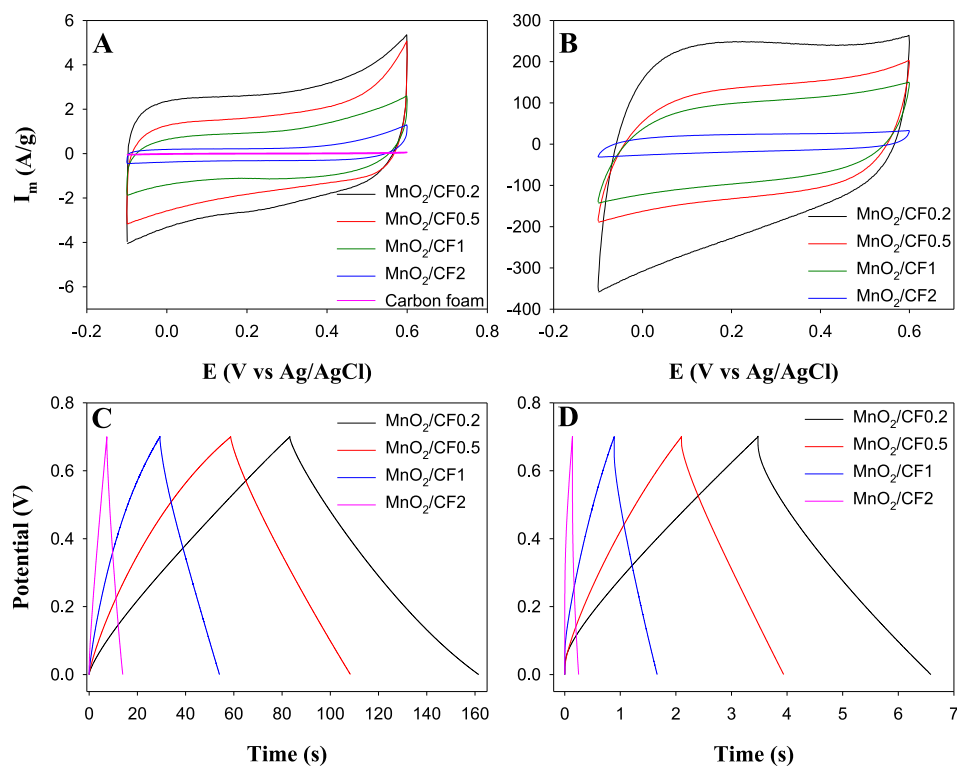
Fig. 6. (A, B) CV curves of the MnO₂/CF composites at the scan rates of 5 mV s^{-1} (A) and 1 V s^{-1} (B) in 1.0 M Na₂SO₄ aqueous electrolyte. (C, D) Galvanostatic charge–discharge curves collected at current densities of 5 A g^{-1} (A) and 80 A g^{-1} (B).
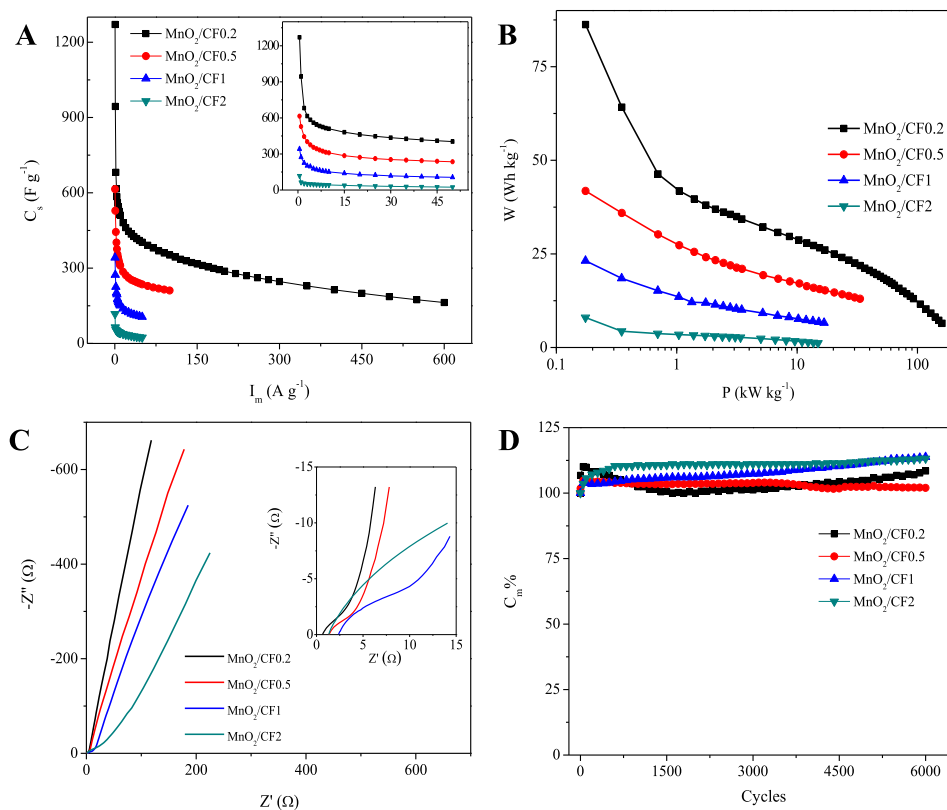
Fig. 7. (A) Specific capacitance plots of the MnO₂/CF composites at different current densities (inset showed C_s vs I_m at low I_m). (B, C) Ragone and Nyquist plots of the supercapacitors based on the MnO₂/CF composites (inset of C showed Nyquist plots at high frequency region). (D) Cycle life curves of the supercapacitors based on MnO₂/CF composites at a current density of 50 A g^{-1}.

Table 1
Comparison of capacitive performance of the supercapacitors based on various binder-free MnO_2 composites presented in literature and the present work.

Samples	C_{max}[a]	v_{max}	I_{max}	W_{max}	P_{max}	T	$C_m\%_T$	Ref.
MnO_2/Au/Te nanowire arrays on CF cloth	930	100	/	80.55	18.61	1000	97	[61]
MnO_2/CNT on ITO	940	1000	/	/	/	1000	88.4	[62]
MnO_2 on ITO	1018	/	30	90.5	17	/	/	[63]
MnO_2/MWCNT/GE/Ni foam	1108.79	1000	>160	391.7	799.84	13,000	97.94	[64]
MnO_2/Ni dendrites/Ni foil	1121	200	100	72	9	1500	81	[65]
MnO_2/Au nanowire/PET	1130	100	50	20	20	5000	90	[66]
MnO_2/nanoporous Au film	1145	/	20	57	16	/	/	[26]
WO_{3-x}/Au/MnO_2/Carbon Fabric	1195	100	15.2	106.4	30.6	5000	110	[67]
MnO_2/CNT/sponge	1230	10,000	100	31	63	10,000	96	[25]
MnO_x/MWCNT sheet	1250	200	10	135	17.4	500	95.5	[68]
3DOM Mn/MnO_x/Au/ITO	1200 ± 60	500	50	140	47.3	2000	96	[69]
MnO_2/HZnO/CF	1260.9	/	9.1	/	/	10,000	87.5	[27]
MnO_2 nanosheets on flexible carbon foam	1270.5	5000	600	86.2	160.0	6000	108.4	This work

[a] C_{max}, maximum specific capacitance, F g^{-1}, calculated based on the mass of MnO_2; v_{max}, maximum scan rate, mV s^{-1}; I_{max}, maximum current density, A g^{-1}; W_{max}, maximum energy density, Wh kg^{-1}; P_{max}, maximum power density, kW kg^{-1}; T, cycles of cycle life test; $C_m\%_T$, retention rate of specific capacitance after cycle life test.

the results of electrochemical impedance spectroscopy (EIS) measurements. As shown in Fig. 7C, each EIS Nyquist plot has a short arc located at high frequencies followed by an inclined line with a slope about 45° and a vertical plot located at low frequencies. The span of the arc is indicative of the charge-transfer resistances of the electrode materials [55]. It can be seen from Fig. 7C that, the spans of the arcs in Nyquist plots increase with the MnO_2 content, which is in accordance with the results of the CV and GCD studies. On the other hand, the straight and nearly vertical lines in the low-frequency region also suggest that the total internal surface area of the porous materials is completely wetted by electrolyte, resulting in the good capacitive behaviors of the MnO_2/CF composites [56].

A long cycle life is another crucial parameter of supercapacitors, which can determine their practical applications. Hence, the stability of the supercapacitors based on the MnO_2/CF composites was tested by cycling at 50 A g^{-1} for 6000 cycles. As showed in Fig. 7D, all the supercapacitors based on the MnO_2/CF composites display excellent stability. The improvements of the specific capacitances upon voltammetric cycling were similar to other manganese oxide-based electrode materials reported previously [57–59]. The increase of the specific capacitance may be due to the activation effect of electrochemical cycling. A recent study showed that small defective or "disordered" regions could be formed in MnO_2 nanostructures upon electrochemical cycling due to the repeated insertion/extraction of the electrolyte ions into/out of the MnO_2 electrode materials [60]. The increased access of the electrolyte ions to the porous electrode materials can thus lead to the increase of capacitance. Table 1 demonstrates the comparison in the capacitive performance of supercapacitors based on various self-supported MnO_2 composites presented in literature and this work. It can be seen that the capacitive performance of the present MnO_2/CF composites surpasses many other excellent 3D binder-free MnO_2 composites. Moreover, compared to the complicated preparation process of other 3D self-supporting MnO_2 composites, the MnO_2/CF composites shown in the present work can be fabricated simply through a green process. Furthermore, in comparison with the high price of other supports, such as porous carbon nanofiber, carbon nanotube arrays/film/paper, graphene gel and nanoporous Au foil, the present carbon foam derived from commercial melamine resin foam is quite cost-effective and it can be produced on large-scale.

4. Conclusion

In summary, a type of ultralight and flexible MnO_2/carbon foam composites were fabricated by growing a layer of MnO_2 nanosheets on the surface of carbon foam via the in situ reaction between aqueous $KMnO_4$ and carbon. Ascribed to the ultrathin and wrinkled MnO_2 nanosheets, the 3D conductive network of carbon foam support, and the hierarchical porous structure of the hybrids, the synthesized MnO_2/CF materials are favorable for electrolyte diffusion and transfer and thus show excellent capacitance performance. It was found that the supercapacitors based on the MnO_2/CF with the thinnest layer of MnO_2 (MnO_2/CF0.2) exhibited the largest specific capacitance of 1270.5 F g^{-1} which is 92.7% of the theoretical value of MnO_2. Moreover, the MnO_2/CF-based supercapacitors exhibit high stability and can endure large current density up to 600 A g^{-1} with high power density of 160.0 kW kg^{-1}. This study provides a facile, scalable and low-cost method for the preparation of ultralight and flexible 3D nanomaterials for supercapacitor electrodes. We expect that this work will open up new opportunities for the application of ultralight and flexible carbon foams in a broad range of emerging electrochemical energy storage and conversion devices, for example, supercapacitors and secondary batteries, to facilitate the corresponding performances.

Appendix A. Supplementary data

Supplementary data related to this article can be found at http://dx.doi.org/10.1016/j.jpowsour.2014.03.137.

References

[1] P. Simon, Y. Gogotsi, Nat. Mater. 7 (2008) 845–854.
[2] P.J. Hall, M. Mirzaeian, S.I. Fletcher, F.B. Sillars, A.J.R. Rennie, G.O. Shitta-Bey, G. Wilson, A. Cruden, R. Carter, Energy Environ. Sci. 3 (2010) 1238–1251.
[3] S.W. Lee, B.M. Gallant, H.R. Byon, P.T. Hammond, Y. Shao-Horn, Energy Environ. Sci. 4 (2011) 1972–1985.
[4] G.M. Wang, X.H. Lu, Y.C. Ling, T. Zhai, H.Y. Wang, Y.X. Tong, Y. Li, ACS Nano 6 (2012) 10296–10302.
[5] W.F. Wei, X.W. Cui, W.X. Chen, D.G. Ivey, Chem. Soc. Rev. 40 (2011) 1697–1721.
[6] Y.P. Zhai, Y.Q. Dou, D.Y. Zhao, P.F. Fulvio, R.T. Mayes, S. Dai, Adv. Mater. 23 (2011) 4828–4850.
[7] G.P. Wang, L. Zhang, J.J. Zhang, Chem. Soc. Rev. 41 (2012) 797–828.
[8] Y.M. He, W.J. Chen, X.D. Li, Z.X. Zhang, J.C. Fu, C.H. Zhao, E.Q. Xie, ACS Nano 7 (2013) 174–182.
[9] X. Huang, Z.Y. Zeng, Z.X. Fan, J.Q. Liu, H. Zhang, Adv. Mater. 24 (2012) 5979–6004.
[10] S.J. He, X.W. Hu, S.L. Chen, H. Hu, M. Hanif, H.Q. Hou, J. Mater. Chem. 22 (2012) 5114–5120.

[11] S.J. He, C.X. Hu, H.Q. Hou, W. Chen, J. Power Sources 246 (2014) 754–761.
[12] S.J. He, L.L. Chen, C.C. Xie, H. Hu, S.L. Chen, M. Hanif, H.Q. Hou, J. Power Sources 243 (2013) 880–886.
[13] Y.X. Zhang, M. Huang, F. Li, X.L. Wang, Z.Q. Wen, J. Power Sources 246 (2014) 449–456.
[14] M.S. Wang, L.Z. Fan, M.A. Huang, J.H. Li, X.H. Qu, J. Power Sources 219 (2012) 29–35.
[15] L.B. Hu, W. Chen, X. Xie, N.A. Liu, Y. Yang, H. Wu, Y. Yao, M. Pasta, H.N. Alshareef, Y. Cui, ACS Nano 5 (2011) 8904–8913.
[16] Z. Gui, H.L. Zhu, E. Gillette, X.G. Han, G.W. Rubloff, L.B. Hu, S.B. Lee, ACS Nano 7 (2013) 6037–6046.
[17] Z.S. Wu, A. Winter, L. Chen, Y. Sun, A. Turchanin, X.L. Feng, K. Mullen, Adv. Mater. 24 (2012) 5130–5135.
[18] Y. Zhao, C.G. Hu, Y. Hu, H.H. Cheng, G.Q. Shi, L.T. Qu, Angew. Chem. Int. Ed. 51 (2012) 11371–11375.
[19] G.K. Wang, X. Sun, F.Y. Lu, H.T. Sun, M.P. Yu, W.L. Jiang, C.S. Liu, J. Lian, Small 8 (2012) 452–459.
[20] J. Biener, M. Stadermann, M. Suss, M.A. Worsley, M.M. Biener, K.A. Rose, T.F. Baumann, Energy Environ. Sci. 4 (2011) 656–667.
[21] Y.M. He, W.J. Chen, C.T. Gao, J.Y. Zhou, X.D. Li, E.Q. Xie, Nanoscale 5 (2013) 8799–8820.
[22] A.L.M. Reddy, S.R. Gowda, M.M. Shaijumon, P.M. Ajayan, Adv. Mater. 24 (2012) 5045–5064.
[23] L.F. Chen, Z.H. Huang, H.W. Liang, Q.F. Guan, S.H. Yu, Adv. Mater. 25 (2013) 4746–4752.
[24] L. Nyholm, G. Nystrom, A. Mihranyan, M. Stromme, Adv. Mater. 23 (2011) 3751–3769.
[25] W. Chen, R.B. Rakhi, L.B. Hu, X. Xie, Y. Cui, H.N. Alshareef, Nano Lett. 11 (2011) 5165–5172.
[26] X.Y. Lang, A. Hirata, T. Fujita, M.W. Chen, Nat. Nanotechnol. 6 (2011) 232–236.
[27] P.H. Yang, X. Xiao, Y.Z. Li, Y. Ding, P.F. Qiang, X.H. Tan, W.J. Mai, Z.Y. Lin, W.Z. Wu, T.Q. Li, H.Y. Jin, P.Y. Liu, J. Zhou, C.P. Wong, Z.L. Wang, ACS Nano 7 (2013) 2617–2626.
[28] Z.P. Chen, W.C. Ren, L.B. Gao, B.L. Liu, S.F. Pei, H.M. Cheng, Nat. Mater. 10 (2011) 424–428.
[29] M.C. Gutierrez, F. Pico, F. Rubio, J.M. Amarilla, F.J. Palomares, M.L. Ferrer, F. del Monte, J.M. Rojo, J. Mater. Chem. 19 (2009) 1236–1240.
[30] M. Antonietti, N. Fechler, T.-P. Fellinger, Chem. Mater. 26 (2014) 196–210.
[31] N. Brun, S.R.S. Prabaharan, C. Surcin, M. Morcrette, H. Deleuze, M. Birot, O. Babot, M.F. Achard, R. Backov, J. Phys. Chem. C 116 (2012) 1408–1421.
[32] M.T. Zheng, Y.L. Liu, S.A. Zhao, W.Q. He, Y. Xiao, D.S. Yuan, Inorg. Chem. 49 (2010) 8674–8683.
[33] H.C. Bi, X. Xie, K.B. Yin, Y.L. Zhou, S. Wan, L.B. He, F. Xu, F. Banhart, L.T. Sun, R.S. Ruoff, Adv. Funct. Mater. 22 (2012) 4421–4425.
[34] X.C. Dong, J. Chen, Y.W. Ma, J. Wang, M.B. Chan-Park, X.M. Liu, L.H. Wang, W. Huang, P. Chen, Chem. Commun. 48 (2012) 10660–10662.
[35] M.A. Worsley, P.J. Pauzauskie, T.Y. Olson, J. Biener, J.H. Satcher, T.F. Baumann, J. Am. Chem. Soc. 132 (2010) 14067–14069.
[36] H.X. Ji, L.L. Zhang, M.T. Pettes, H.F. Li, S.S. Chen, L. Shi, R. Piner, R.S. Ruoff, Nano Lett. 12 (2012) 2446–2451.
[37] S. Nardecchia, D. Carriazo, M.L. Ferrer, M.C. Gutierrez, F. del Monte, Chem. Soc. Rev. 42 (2013) 794–830.
[38] Z.Y. Wu, C. Li, H.W. Liang, J.F. Chen, S.H. Yu, Angew. Chem. Int. Ed. 52 (2013) 2925–2929.
[39] M. Toupin, T. Brousse, D. Belanger, Chem. Mater. 16 (2004) 3184–3190.
[40] Z.W. Xu, Z. Li, C.M.B. Holt, X.H. Tan, H.L. Wang, B.S. Amirkhiz, T. Stephenson, D. Mitlin, J. Phys. Chem. Lett. 3 (2012) 2928–2933.
[41] S. Chen, H. Hou, F. Harnisch, S.A. Patil, A.A. Carmona-Martinez, S. Agarwal, Y. Zhang, S. Sinha-Ray, A.L. Yarin, A. Greiner, U. Schroder, Energy Environ. Sci. 4 (2011) 1417–1421.
[42] S. Chen, G. He, H. Hu, S. Jin, Y. Zhou, Y. He, S. He, F. Zhao, H. Hou, Energy Environ. Sci. 6 (2013) 2435–2439.
[43] Z. Liu, R. Ma, Y. Ebina, K. Takada, T. Sasaki, Chem. Mater. 19 (2007) 6504–6512.
[44] Y. Luo, J. Jiang, W. Zhou, H. Yang, J. Luo, X. Qi, H. Zhang, D.Y.W. Yu, C.M. Li, T. Yu, J. Mater. Chem. 22 (2012) 8634–8640.
[45] H.Q. Wang, G.F. Yang, Q.Y. Li, X.X. Zhong, F.P. Wang, Z.S. Li, Y.H. Li, New J. Chem. 35 (2011) 469–475.
[46] P. Ragupathy, D.H. Park, G. Campet, H.N. Vasan, S.-J. Hwang, J.-H. Choy, N. Munichandraiah, J. Phys. Chem. C 113 (2009) 6303–6309.
[47] J. Yan, Z. Fan, T. Wei, W. Qian, M. Zhang, F. Wei, Carbon 48 (2010) 3825–3833.
[48] Z. Fan, J. Yan, T. Wei, L. Zhi, G. Ning, T. Li, F. Wei, Adv. Funct. Mater. 21 (2011) 2366–2375.
[49] C.T. Hsieh, H. Teng, W.Y. Chen, Y.S. Cheng, Carbon 48 (2010) 4219–4229.
[50] J.G. Wang, Y. Yang, Z.H. Huang, F.Y. Kang, J. Power Sources 224 (2013) 86–92.
[51] R.B. Rakhi, W. Chen, D. Cha, H.N. Alshareef, Adv. Energy Mater. 2 (2012) 381–389.
[52] J. Zhang, X.S. Zhao, Carbon 52 (2013) 1–9.
[53] J. Han, L. Li, P. Fang, R. Guo, J. Phys. Chem. C 116 (2012) 15900–15907.
[54] S.C. Pang, M.A. Anderson, T.W. Chapman, J. Electrochem. Soc. 147 (2000) 444–450.
[55] Z. Weng, Y. Su, D.W. Wang, F. Li, J. Du, H.M. Cheng, Adv. Energy Mater. 1 (2011) 917–922.
[56] E. Ra, E. Raymundo-Pinero, Y. Lee, F. Beguin, Carbon 47 (2009) 2984–2992.
[57] M. Toupin, T. Brousse, D. Bélanger, Chem. Mater. 14 (2002) 3946–3952.
[58] H. Jiang, L. Yang, C. Li, C. Yan, P.S. Lee, J. Ma, Energy Environ. Sci. 4 (2011) 1813–1819.
[59] C.-Y. Chen, C.-Y. Fan, M.-T. Lee, J.-K. Chang, J. Mater. Chem. 22 (2012) 7697–7700.
[60] W. Chen, R.B. Rakhi, Q.X. Wang, M.N. Hedhili, H.N. Alshareef, Adv. Funct. Mater. (2014), http://dx.doi.org/10.1002/adfm.201303508.
[61] J. Cao, M. Safdar, Z. Wang, J. He, J. Mater. Chem. A 1 (2013) 10024–10029.
[62] S.W. Lee, J. Kim, S. Chen, P.T. Hammond, Y. Shao-Horn, ACS Nano 4 (2010) 3889–3896.
[63] Y. Zhang, J. Li, F. Kang, F. Gao, X. Wang, Int. J. Hydrogen Energy 37 (2012) 860–866.
[64] W. Wang, S.R. Guo, K.N. Bozhilov, D. Yan, M. Ozkan, C.S. Ozkan, Small 9 (2013) 3714–3721.
[65] Z. Sun, Z. Firdoz, E. Ying-Xuan Yap, L. Li, X. Lu, Nanoscale 5 (2013) 4379–4387.
[66] Y.L. Chen, P.C. Chen, T.L. Chen, C.Y. Lee, H.T. Chiu, J. Mater. Chem. A 1 (2013) 13301–13307.
[67] X. Lu, T. Zhai, X. Zhang, Y. Shen, L. Yuan, B. Hu, L. Gong, J. Chen, Y. Gao, J. Zhou, Y. Tong, Z.L. Wang, Adv. Mater. 24 (2012) 938–944.
[68] J.H. Kim, K.H. Lee, L.J. Overzet, G.S. Lee, Nano Lett. 11 (2011) 2611–2617.
[69] M.J. Deng, P.J. Ho, C.Z. Song, S.A. Chen, J.F. Lee, J.M. Chen, K.T. Lu, Energy Environ. Sci. 6 (2013) 2178–2185.